An Ordinary State-Based Peridynamic Model for Toughness Enhancement of Brittle Materials through Drilling Stop-Holes

Mohammad Naqib Rahimi[1,2,3], Adnan Kefal[1,2,3,4,*], Mehmet Yildiz[1,2,3], and Erkan Oterkus[5]

[1] Faculty of Engineering and Natural Sciences, Sabanci University, Tuzla, Istanbul 34956, Turkey

[2] Integrated Manufacturing Technologies Research and Application Center, Sabanci University, Tuzla, 34956, Istanbul, Turkey

[3] Composite Technologies Center of Excellence, Istanbul Technology Development Zone, Sabanci University-Kordsa, Pendik, Istanbul 34906, Turkey

[4] Faculty of Naval Architecture and Ocean Engineering, Istanbul Technical University, Maslak-Sariyer 34469, Istanbul, Turkey.

[5] Department of Naval Architecture, Ocean and Marine Engineering, University of Strathclyde, Glasgow G4 0LZ, United Kingdom

* Corresponding author: adnankefal@sabanciuniv.edu; kefaladnan@itu.edu.tr

Abstract

In this paper, the ordinary state-based peridynamic (OSB) is used to simulate and study the effects of different-shaped stop-holes with different combinations on crack dynamics in brittle materials in order to establish a detailed knowledge about the toughening effect of internal features that can be in the form of holes and pores. Using the OSB analyses, a new easy-to-apply technique is introduced to toughen the materials against crack propagations. As a first case study, the high accuracy of peridynamic approach in damage prediction is demonstrated through solving a collection of numerical and experimental benchmark problems. Moreover, the *bi-hole*, *parabolic*, *branched*, *bi-parabolic*, and *mixed-parabolic* combinations of stop-holes under tensile loading, and the *T-shape*, *I-shape*, *bi-linear*, *linear*, and *linear-parabolic* combinations of stop-holes under shear loading are suggested for notably enhancing material toughness and are practically and functionally compared with each other. Generally, the suggested geometries are proven to be highly effective on toughness enhancement of materials with a relative ease of implementation, in comparison to other internal features such as micro-cracks. In addition, a further case study is carried out on the effects of the distance of stop-holes from the initial crack-tip on crack dynamics and material toughness, in which it is observed that every hole has a specific μ-range, and thus, the crack dynamics are affected by the hole if and only if the crack enters this range. Overall, the arrestment and accelerating effects of the stop-holes on crack dynamics are carefully explained numerically and conceptually, which will help engineers and designers to maximize the positive effects of stop-holes on material toughness and design a tougher micro-structural material using easily applied defects.

Keywords: Peridynamics; fracture mechanics; non-local approaches; stop-holes; material toughening.

1. Introduction

Over the last few centuries, a large collection of research studies has been dedicated to understanding the fracture mechanics of engineering materials, some can even be traced back to the 1770's [1]. However, in today's engineering society, almost every engineering field still suffers from the lack of predicting the potential occurrence of crack propagations. Depending on the environmental/operational conditions of an engineering structure, load-bearing components of the structure may be subjected to extreme loading conditions, thus leading to emergence of the *so-called* micro-cracks. These micro-cracks can either grow independently or coalesce to form various macro-cracks, which eventually cause a complete failure of the structure. The formation of a complete rupture in a very short amount of time (e.g., microseconds) is a particular study case of fracture mechanics, which is referred to as "brittle fracture" and commonly present in brittle materials. This kind of failure bears a high potential risk to human safety, increase environmental pollution, and cause crucial financial losses [2–4]. Therefore, especially after the industrial revolution, fracture mechanics of brittle materials has gained a great deal of interest.

Numerous solutions have been suggested to reduce the crack growth rate of brittle fracture. One of which is to lessen the stress concentration at the crack tip through making a perforation, i.e., stop-hole. Among early studies available in the literature, Broek [5] experimentally investigated the effect of stop-holes on crack dynamics in a continuum by allocating a stop-hole on propagation path of a crack. According to his results, the arrestment effect of the hole on the crack is balanced by the crack growth acceleration caused by the hole. On the other hand, Miyagawa and Nisitani [6] later demonstrated the superior effect of holes on crack growth life by extending Broek's investigation to two and four hole combinations located ahead of a pre-existing crack. In fact, any growing crack tends to propagate with an increasing velocity towards a hole located in the vicinity of its tip or along its original propagation path. Moreover, the existence of holes in a body affects the stress intensity factor of growing cracks [7]. A crack running towards a hole has a considerably larger stress intensity factor, further accelerating the crack propagation. However, when a crack joins the hole, the hole arrests the growing crack for a significant amount of time causing the crack to release its strain energy accumulation. This eventually leads to a longer crack growth life. Hence, crack dynamics (i.e., acceleration and velocity of crack propagation and crack growth life) are substantially influenced if any discontinuity, such as a hole, exists in the continuum [8].

When a weak zone (i.e., *so-called* stop-hole) is introduced into a homogenous material, the mechanical response of the material will involve relatively non-homogeneous effects, especially near the weak zone. Therefore, crack dynamics in non-homogeneous regions of materials are different from the ones in homogenous regions. Recently, Carlsson and Isaksson [9] investigated the effect of this heterogeneity on crack dynamics using the dynamic phase-field method (DPF) introduced in [10]. To model the existence and propagation of a crack, the

phase-field method requires an external differential equation to be solved along with the governing equations of classical continuum mechanics. This usage of the external equation is one of the main deficits of phase-field method [11]. A robust non-local continuum theory, originally introduced by Silling [12], named as peridynamics (PD), however, eliminates the shortcomings of classical continuum theory, especially the ones pertaining to modelling of solid continuums involving any discontinuity such as cracks. Although the peridynamic theory was first introduced in the 2000's and applied to solid mechanics of isotropic materials [12], since then it has been further developed for other engineering applications including modelling of composites [13], multi-physics problems [14], heat transfer [15], etc. For example, De Meo et al. [16] introduced a computational PD model for fracture behaviour of cracked HSLA steel subjected to a corrosive environment. Recently, Kefal et al. [17] used peridynamic theory for structural topology optimizations of engineering structures with and without cracks. More recently, the PD-TO approach [17] has been extended for continuous density-based topology optimization [18]. Another work on the PD application is the failure model developed by Ghajari et al. [19] for orthotropic materials. And yet in another track, Wang et. al. [20] developed a peridynamic formulation for thermo-visco-plastic deformation and impact fracture. Thus, with the help of these and other significant contributions not listed, PD approach has gained a capability to solve diverse applications of engineering problems for different materials [21–39]. Reader may also refer to the study of Javili et al. [40] for a detailed review on PD theory.

In general, there are three different types of peridynamic theory, namely bond-based (BB) PD, ordinary state-based (OSB) PD, and non-ordinary state-based (NOSB) PD. In the bond-based PD formulation, it is assumed that the interaction forces between two material points are equal in magnitude and opposite in direction. Therefore, the bond-based PD can be applicable only to analyses of materials having Poisson's ratio of *1/4* in three dimensions and *1/3* in two dimensions [12]. However, this limitation was later circumvented by the introduction of the OSB and NOSB forms of peridynamic theory [26]. In OSB type of PD, it is assumed that the direction of the pair forces is along the interaction direction, but their magnitudes may vary. The NOSB, more generally, considers the pair forces between two material points to be different in both magnitude and direction [26]. In all of the PD types, the interactions between material points are independent of each other, enabling PD to be applied to materials with discontinuities, such as cracks, with no usage of complex mathematical formulations [12]. This ease of implementation makes the PD formulation advantageous for analysis of static and/or dynamic crack propagation problems.

Recently, Vazic et al. [41] used the bond-based (BB) PD formulation to investigate the effect of the presence of parallel micro-cracks on dynamics of a main crack and their effects on the toughness enhancement of the poly methyl methacrylate (PMMA) material. According to their results, both positive and negative influence rate of micro-cracks are observed on the velocity of main-crack propagation and material toughness. Most recently, Basoglu et al. [42] extended Vazic et al.'s work by examining different combinations of linear and curvilinear micro-cracks in order to determine the most effective intentionally applied micro-crack combination on material toughness by means of micro-macro crack dynamics. The crescent-like combinations

of micro cracks in the vicinity of the main crack tip have proven to be effective in reducing the main crack propagation velocity [42]. However, the suggested combinations of micro-cracks can be difficult to implement to a real-world material. Furthermore, the usage of BB in the analysis of materials having a Poisson's ratio other than *1/3* (in two dimensions) or *1/4* (in three dimensions) can sometimes cause significant error.

In the present study, the OSB formulation of PD is used to address the above-mentioned issues and to simulate more realistic path of crack propagation in materials with different Poisson's ratios. In addition, instead of micro-cracks, the effects of stop-holes are investigated on crack dynamics and toughness of materials given that stop-holes can be realistically created. Since the presence of stop-holes can reduce the weight of the structure and is relatively easy to implement, it can be more economical to use as a toughening mechanism of the engineering parts.

Several researchers have investigated the arresting effect of stop-holes drilled at the vicinity of the pre-existing crack tip and have suggested drilling stop-holes as a repairing technique for the cracked parts of structures. For instance, Fu et. al. [43] investigated the effect of one and two drilled stop-holes on fatigue life of steel bridge deck. They concluded that a higher fatigue life can be achieved if a stop-hole is drilled near the crack tip. They also indicated that a larger diameter of the drilled stop-hole causes a longer fatigue life by further reducing the stress concentration. Ghfiri et al. [44] used the hole-expansion method to introduce residual stresses that can reduce the effective stress around the crack tip. They drilled a stop-hole in aluminium sheet specimens and investigated its crack growth arresting behaviour under axial fatigue test. For some of the specimens, they cold-expanded the stop-hole diameter and compared its effect on fatigue life. According to their results, an expanded stop-hole had a higher crack growth arresting effect than that of non-expanded stop-holes. Similarly, Song et. al. [45] used stop-hole drilling procedure to improve the fatigue life of aluminium alloys and stainless steel. Recently, Ferdous et al. [46] have investigated the effect of four uniformly distributed stop-holes on fatigue life of specimens. Aside the above listed experimental works, Ayatollahi et al. [47] numerically investigated the effect of drilling one stop-hole based on classical fracture mechanics model. However, the main variable of their numerical investigation was the size of the stop-hole. To optimize the shape of stop-hole, in a unique track, Fanni et. al. [48] used structural optimization technique by utilizing finite element method.

Although several of the above researchers have numerically/experimentally studied the effects of one circular stop-hole on crack propagation path and fatigue life, to the best of authors' knowledge, no literature has been dedicated to the investigation of the effects of the "linear" and/or "non-linear" combinations of more than one stop-hole on material toughness under "tensile" and "shear" loadings. Hence, the main novelty of the current study is to present a detailed knowledge about the various toughening effects of stop-hole combinations through the OSB-PD analyses, while introducing a new approach of implementing linear and/or nonlinear combinations of stop-holes as a material toughening technique.

The rest of the paper is structured as follows; a brief mathematical description of OSB-PD theory is given in Section 2. In Section 3, a computational application of the OSB-PD theory is performed and toughness enhancement in brittle materials via stop-holes under shear and tensile loading is investigated. It is shown that the relative positions of stop-holes have a notable influence on toughness enhancement. Moreover, the toughness of the material can be tailored through adjusting the locations of the stop holes. It is later indicated that every stop-hole has an influence range (μ-range) beyond which the crack dynamics are not affected. Furthermore, the experimental/numerical benchmark studies reported in [9] and [49] are revisited whereby the accuracy of the OSB approach is demonstrated and compared with the DPF models. Finally, the advantages, superior predictive capabilities, and concluding remarks of the current approach are elaborated in Section 4.

2. Formulation of Ordinary-State Based Peridynamics

Peridynamics is a mesh-free approach originally introduced by Silling in 2000 [12]. The PD approach is referred to as the non-local form of classical continuum mechanics (CCM) or the shrunken form of molecular dynamics (MD). Peridynamic theory uses integro-differential equations rather than the classical spatial derivatives of stress components; thus, it is an ideal approach for fracture mechanics problems involving discontinuities (e.g., cracks). In PD, a continuum is introduced by a set of infinitesimal volumes, called material points, which interact to each other in a non-local manner. The range of this interaction is named as horizon, δ, and the interactions are called the PD bonds. All material points located within the distance δ of point i constitute its family members, H_i. For a three-dimensional continuum, H is a spherical set of material points with a radius of δ, while it reduces to a circular domain in a two-dimensional case as depicted in *Figure 1*.

The governing equation of motion in PD is defined as the integral form of pair forces of the interacting i and j material points, $\mathbf{t}_{ij}$ and $\mathbf{t}_{ji}$. Hence, for any material point i, initially located at $\mathbf{X}_i$, the PD equation of motion can be written as:

$$\rho_i(\mathbf{X}_i)\ddot{\mathbf{u}}_i(\mathbf{X}_i,t) = \int_{H_i}\left[\mathbf{t}_{ij}(\mathbf{u}_j-\mathbf{u}_i,\boldsymbol{\xi}_{ji}) - \mathbf{t}_{ji}(\mathbf{u}_i-\mathbf{u}_j,\boldsymbol{\xi}_{ij})\right]dH_i + \mathbf{B}_i(\mathbf{X}_i,t) \tag{1}$$

where the $\boldsymbol{\xi}_{ij} = \mathbf{X}_j - \mathbf{X}_i$ vector defines the relative initial position of the i and j material points and the vectors $\mathbf{u}_i$ and $\mathbf{u}_j$ denote their displacements, respectively (*Figure 2*). By discretizing the body into subdomains (material points and families) and applying the Gaussian quadrature [50], Eq. (1) can be rewritten in its discrete form as follows:

$$\rho_i(\mathbf{X}_i)\ddot{\mathbf{u}}_i(\mathbf{X}_i,t) = \sum_{j=1}^{N}\left[\mathbf{t}_{ij}(\mathbf{u}_j-\mathbf{u}_i,\boldsymbol{\xi}_{ij}) - \mathbf{t}_{ji}(\mathbf{u}_i-\mathbf{u}_j,\boldsymbol{\xi}_{ij})\right]V_j + \mathbf{B}_i(\mathbf{X}_i,t) \tag{2}$$

where the parameters ρ, $\ddot{\mathbf{u}}$ and $\mathbf{B}$ are the density, acceleration, and body force, respectively. V_j denotes the discrete volume of the point j and N is the number of points located within the

horizon of the point *i*. Note that for a cubic subdomain the Gaussian integration point is located at the centre of the cube. The terms $\mathbf{t}_{ij}$ and $\mathbf{t}_{ji}$ are named as the force density vectors and can be expressed as follows:

$$\mathbf{t}_{ij}(\mathbf{u}_j - \mathbf{u}_i, \boldsymbol{\xi}_{ij}, t) = \frac{1}{2} A\hat{\mathbf{e}} \tag{3}$$

$$\mathbf{t}_{ji}(\mathbf{u}_i - \mathbf{u}_j, \boldsymbol{\xi}_{ji}, t) = -\frac{1}{2} B\hat{\mathbf{e}} \tag{4}$$

with the direction

$$\hat{\mathbf{e}} = \frac{\boldsymbol{\eta}_{ij}}{|\boldsymbol{\eta}_{ij}|} \tag{5}$$

where the vector $\boldsymbol{\eta}_{ij} = \mathbf{Y}_j - \mathbf{Y}_i$ describes the relative final position of material points *i* and *j* (*Figure 2*).

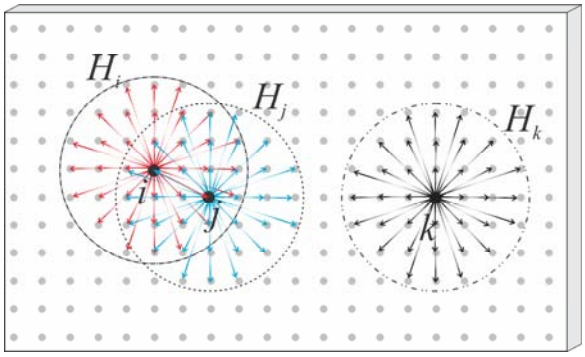

Figure 1) A two-dimensional discretization of PD continuum

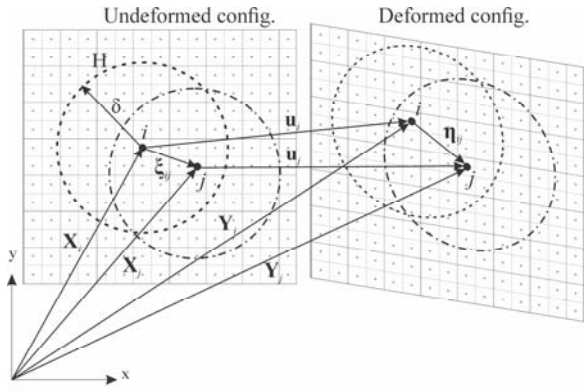

Figure 2) A two-dimensional representation of the deformed and undeformed states of PD

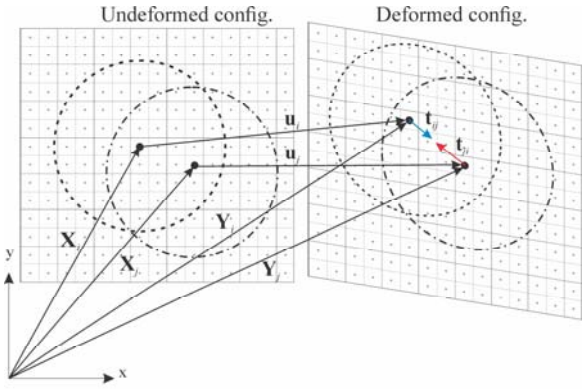

Figure 3) Pair forces of material point i and j

In order to determine the auxiliary parameters A and B in Eqs. (3) and (4), it is necessary to establish a relation between force density vectors and strain energy density. For this purpose, consider the bond interaction between two material points as an elastic spring; thus, the change in the length of the bond results in a micro potential. By integrating these micro potentials over the family H_i, the strain energy density, $W(\mathbf{X}_i)$, for material point i can be calculated. On the other hand, by applying the Lagrangian equation [51] to the principle of virtual work, the following relation can be achieved [27]:

$$\mathbf{t}_{ij}(\mathbf{u}_j - \mathbf{u}_i, \boldsymbol{\xi}_{ij}, t) \approx \frac{\partial W(\mathbf{X}_i)}{\partial(|\boldsymbol{\eta}_{ij}|)}\hat{\mathbf{e}} \tag{6}$$

Hence, the discrete expression for strain energy density can be written in its final form as:

$$W(\mathbf{X}_i) = a\theta_i^2 + b\delta\sum_{j=1}^{N} S_{ij}{}^2 |\boldsymbol{\xi}_{ij}| V_j \tag{7}$$

with

$$\theta_i = d\delta\sum_{j=1}^{N} S_{ij}\left(\frac{\boldsymbol{\eta}_{ij}}{|\boldsymbol{\eta}_{ij}|}\cdot\frac{\boldsymbol{\xi}_{ij}}{|\boldsymbol{\xi}_{ij}|}\right)V_j \tag{8}$$

Here, a, b and d in Eqs. (7) and (8) are the PD parameters dependent on material properties as well as horizon size and can be written for a two-dimensional domain as [27]:

$$a = \frac{1}{2}(\kappa - 2\mu), \qquad b = \frac{6\mu}{\pi h\delta^4}, \qquad d = \frac{2}{\pi h\delta^3} \tag{9}$$

where h is the thickness and κ and μ are the bulk and shear modulus of material, respectively. The parameter, θ_i, denotes the PD dilatation of material point i. The stretch, S_{ij}, of the bond between material points i and j can be calculated as:

$$S_{ij} = \frac{\left|\boldsymbol{\eta}_{ij}\right| - \left|\boldsymbol{\xi}_{ij}\right|}{\left|\boldsymbol{\xi}_{ij}\right|} \tag{10}$$

where the $|...|$ operator denotes the magnitude of the related vector. By substituting Eqs. (8-10) into Eq. (7) and taking the derivative with respect to $\left|\boldsymbol{\eta}_{ij}\right|$, one can obtain the parameters A and B as

$$A = \left(\mu_{ij}\right) 4 \frac{\delta}{\left|\boldsymbol{\xi}_{ij}\right|} \left\{ d \left(\frac{\boldsymbol{\eta}_{ij}}{\left|\boldsymbol{\eta}_{ij}\right|} \cdot \frac{\boldsymbol{\xi}_{ij}}{\left|\boldsymbol{\xi}_{ij}\right|} \right) a\theta_i + b \left|\boldsymbol{\xi}_{ij}\right| S_{ij} \right\} \tag{11}$$

$$B = \left(\mu_{ij}\right) 4 \frac{\delta}{\left|\boldsymbol{\xi}_{ji}\right|} \left\{ d \left(\frac{\boldsymbol{\eta}_{ij}}{\left|\boldsymbol{\eta}_{ij}\right|} \cdot \frac{\boldsymbol{\xi}_{ij}}{\left|\boldsymbol{\xi}_{ij}\right|} \right) a\theta_j + b \left|\boldsymbol{\xi}_{ji}\right| S_{ji} \right\} \tag{12}$$

with μ_{ij} being an irreversible control parameter over the failure of the bond between material points i and j. Thus, it is

$$\mu_{ij} = \begin{cases} 1 & \text{if } \mathrm{S}_{ij} < S_0 \\ 0 & \text{otherwise} \end{cases} \tag{13}$$

Where S_0 represents the critical stretch, which can be calculated as [27]:

$$S_0 = \sqrt{\frac{G_c}{bh\delta^5 + \frac{8}{9} ad^2 h^2 \delta^7}} \tag{14}$$

for the two-dimensional analysis. Here, the critical energy release rate, G_c, is an important material property which can be determined using the combination of experimental and statistical methods [52–54] . Furthermore, a damage parameter, φ, can also be introduced to track the damage of material points as the crack grows throughout the body in time as [27]:

$$\varphi_i = 1 - \frac{\sum_{j=1}^{N} \mu_{ij} V_j}{\sum_{j=1}^{N} V_j} \tag{15}$$

Thus, the damage parameter takes the value of unity if all bonds of the material point are broken while it becomes zero for material points with no broken bonds. Finally, using the standard von Neumann stability analysis [55] a stable time-step size, dt, can be chosen, as in Eq. (16), to integrate the PD equation of motion through time [27].

$$dt = 0.8 \sqrt{\frac{\rho}{2\pi b \delta^3}} \tag{16}$$

3. Numerical Examples

In this section, five different examples are investigated utilizing the aforementioned OSB peridynamic formulation. The OSB-PD formulation is implemented as an in-house code utilizing the C++ programming language. All the OSB analyses are carried out for the PMMA material, which is considered to have linear-elastic and brittle properties. First, the original numerical and experimental work of Carlsson and Isaksson [9] is revisited. Through the analysis of this problem, we validate our OSB-PD implementation and demonstrate its high accuracy of modeling the effects of holes in the bodies with discontinuities/cracks. As a second validation case, the experimental work of Ayatullahi and Aliha [49] is solved to validate the accuracy of OSB-PD implementation under mode I, mode II and mixed mode I-II loading conditions. In the third and fourth case studies, the effect of different combinations of stop-holes on crack dynamics are subsequently investigated by using the OSB-PD algorithm to increase the material toughness of the brittle materials subjected to tensile and shear loadings. Finally, a further case study is conducted to examine the effect of the distance of stop-holes from crack tip on crack dynamics and associated material toughening mechanism.

3.1 Benchmark problem

This problem was originally solved by Carlsson and Isaksson using dynamic phase field method (DPF) and was compared with experimental results [9]. The authors investigated the effects of circular holes on crack propagation path, which are placed in a parallel combination to a pre-existing crack with a length of $l=2$ *mm* in a PMMA plate with dimensions $L \times W = 50$ *mm x 25 mm*. The material properties of PMMA are given in *Table 1*. Four different geometries were considered for the plate and were subjected to a uniaxial loading of crosshead velocity of *5 mm/s* (*Figure 4*). Herein, the problem is solved using OSB-PD approach to validate the present algorithm and its implementation on similar cases.

Table 1) Material properties of PMMA

E	ν	ρ	G_c
3.24 GPa	0.35	1190 Kg/m^3	200 J/m^2

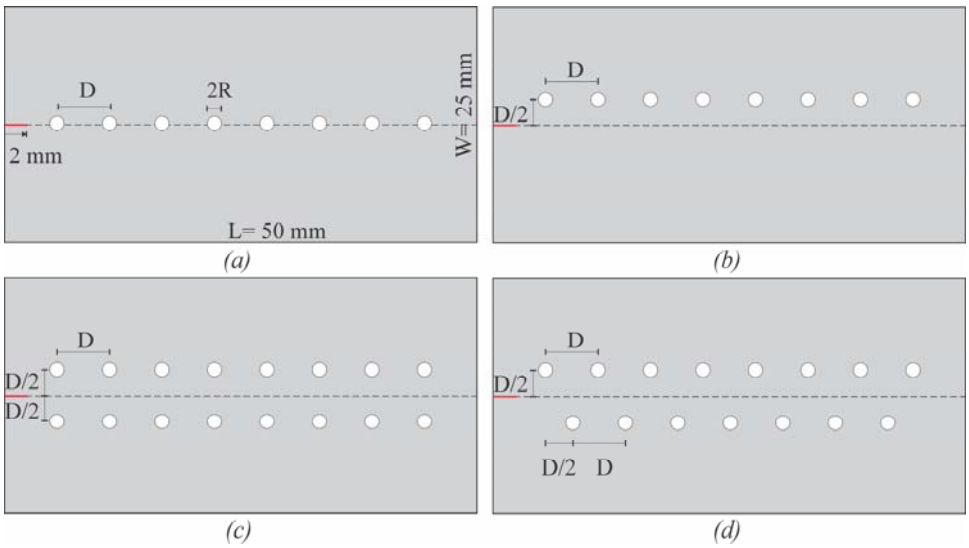

Figure 4) Geometric properties of the plates originally solved by Carlsson and Isaksson [9] *with 2R=3L/100 and D=L/9*

The plate is uniformly discretised using *200x100* material points along length and width directions, respectively, leading to uniform particle spacing of *dx=0.25 mm*. In order to reduce the computation time, the crosshead velocity boundary condition is applied as *300 mm/s* and is deployed on a virtual boundary of three layers (of material points) at the top and the bottom boundaries of the plates having a thickness equal to *dx*.

The crack in *geometries a*, *b*, *c*, and *d* starts to propagate after approximately 2900^{th} time-step. To gain foreknowledge of the crack propagation paths and understand physical interface of the crack growth, we investigate the displacement and strain energy distributions of the geometries at an instant before pre-existing crack's propagation, i.e., 2600^{th} time-step. Accordingly, the *x* and *y* displacements of *geometries a*, *b*, *c*, and *d* at 2600^{th} time-step are presented in *Figure 6*, where the spatial variation of the displacement contours precisely matches with the expected physical/mechanical response of the tensile loading. Moreover, a high vertical displacement jump is observed in the region of the pre-existing crack demonstrating the crack opening in this region which finally leads to a mode-I fracture loading. In fact, any increase in relative displacement of two adjacent material points causes an increase in strain energy density of the bond between these points. If the strain energy density (or stretch) of a bond exceeds the critical strain energy density (or critical stretch), the bond breaks. *Figure 7* shows the distribution of the strain energy density over the plate at 2600^{th} time-step for each geometry. As can be seen, micro-cracks are likely to be born from perimeter of the holes in *geometry b*, *c* and *d* since the strain energy densities of the points near the holes are relatively higher than the ones located in the far field. However, the experimental results demonstrate no generation of new cracks from the holes (*Figure 5*). This may be attributed to the increased fracture toughness of cut-out surfaces of the holes due to the drilling process [56]. To comply with such phase change of material, the critical stretch value for two material layers around the holes are doubled for all

geometries. This prevents the generation of micro-crack formations around the hole, thus resulting in a more elastic material properties in this region. However, if the spacing between material points is small enough (a finer mesh), the region with increased elasticity becomes very small, thus, providing a negligible effect on behaviour of the main crack.

The above results of OSB analyses are compared with those of DPF analysis and experiment [9] in *Figure 5*. A superior prediction of the crack paths in *geometries a* and *b* is obtained using the present OSB-PD implementation. OSB was able to capture the branching effect of the crack in *geometry a*, which is much similar to the experimental result where the branching effect is seen after the third and the fifth holes (*Figure 5*). However, a small amount of crack branching is also predicted in other regions of the crack propagation path in *geometry a*, which may be attributed to the different velocity boundary conditions applied herein [31]. Furthermore, the result obtained for *geometry b* using OSB approach sufficiently indicates the higher accuracy of the prediction of the crack path by OSB analyses. In *geometry b*, the propagation path predicted by DPF eventually joins the holes whereas the OSB method predicts an almost parallel propagation path to the horizontal, which is quite similar to the real propagation path of the crack observed in experiment.

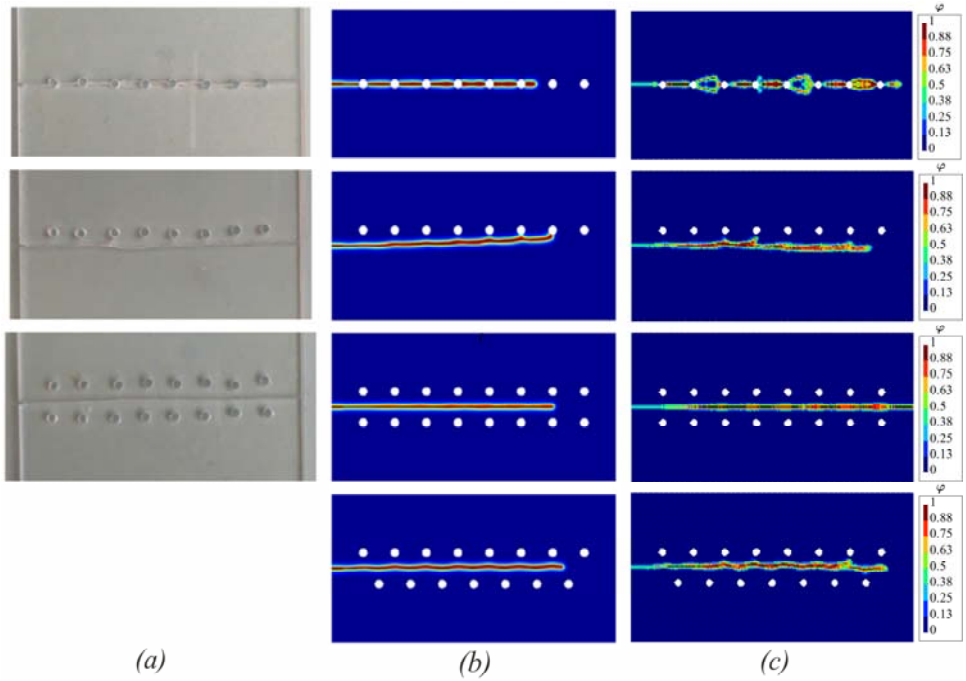

Figure 5) Comparison of the results obtained from a) experiments [9], b) DPF [9] and c) OSB analyses where the first row represents geometry a; second row represents geometry b; third row represents geometry c and fourth row represents geometry d

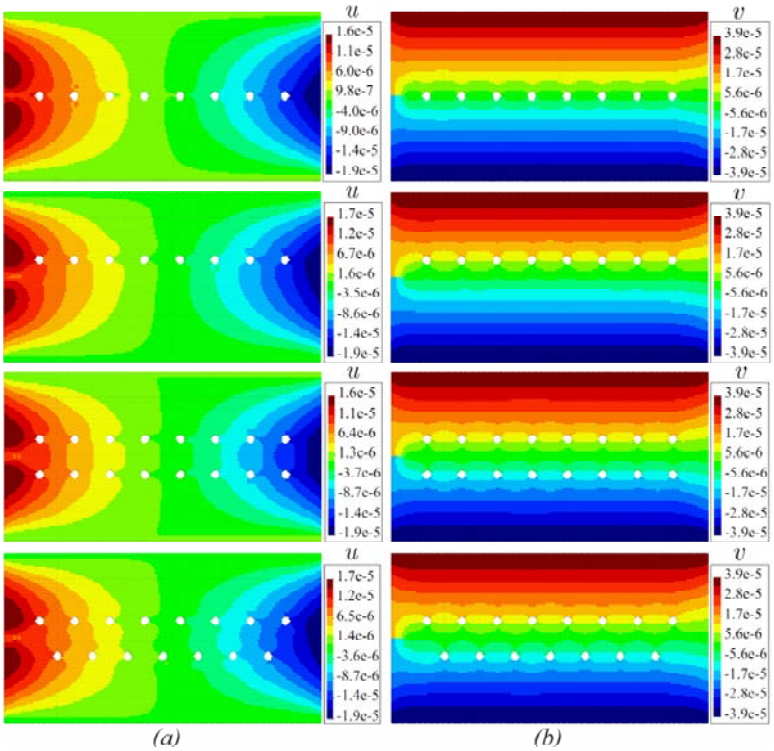

Figure 6) Displacement in a) x-direction, u [m], and b) y-direction, v [m], of geometry a, b, c, and d at 2600th time-step

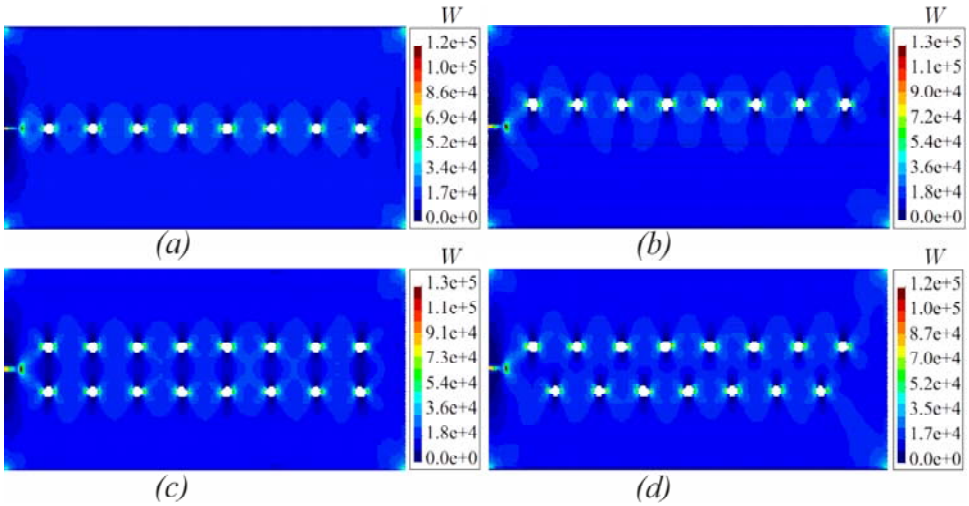

Figure 7) Strain energy densities, W [J/m3], of the geometries at 2600th time-step

3.2 Diagonally Loaded Square Plate (DLSP)

To further indicate the accuracy and robustness of present algorithm, a fracture test configuration, named as the "DLSP (Diagonally Loaded Square Plate) specimen [49]", is solved under pure mode-I, pure mode-II, and mixed mode I-II fracture loading conditions and is validated against the experimental results. The modelled geometry has the following dimensions and crack orientations: side length of $2w = 150mm$, thickness of $h = 5\ mm$, and a crack with an initial length of $2a = 45\ mm$ located at the centre of the plate at an angle of α.

The material properties of the plate are given in *Table 2*. A set of numerical configurations is analysed under a velocity boundary condition of $V = 10^{-8}\, m/s$ to achieve a quasi-static loading condition. This velocity condition is applied to three layers of material points around the upper and lower circular cut-outs of the plate as depicted in *Figure 8*. The DLSP domain is discretized into $150x150$ points with particle spacing of $dx = 1.0\, mm$. The quasi-static boundary condition is imposed using adaptive dynamic relaxation method [33]. The analyses are run for a total of *40 000* time-steps with a time-step size of $dt = 1s$.

Table 2) Material properties of the DLSP test specimen

E	ν	P	Gc
2.94 GPa	0.38	1200 Kg/m3	602 J/m2

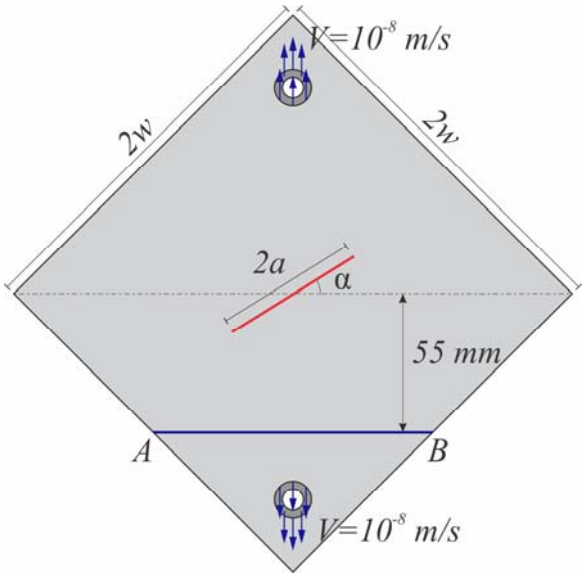

Figure 8) Geometric properties of DLSP specimen

Figure 9 shows a comparison of the final crack path obtained from OSB analyses with the experimental ones for α values of $0^o, 15^o, 30^o, 45^o$ and 62.5^o. The specific value of $\alpha = 0^o$ corresponds to the pure mode-I loading condition. The angle, $\alpha = 62.5^o$ with ${}^{a}/_{w} = 0.3$ corresponds to a pure mode-II loading whereas the α values between 0 and 62.5 leads to the mixed mode I-II. The failure load is monitored by summing the forces over the interactions passing through the line $\overline{AB}$ and compared with the experimental results in *Figure 10*. The results obtained from the OSB analyses are in a good agreement with the ones of experiments in terms of both the final crack path and internal forces. Hence, it can be stated that the algorithm used herein is able to model the crack dynamics reliably under any in-plane loading conditions.

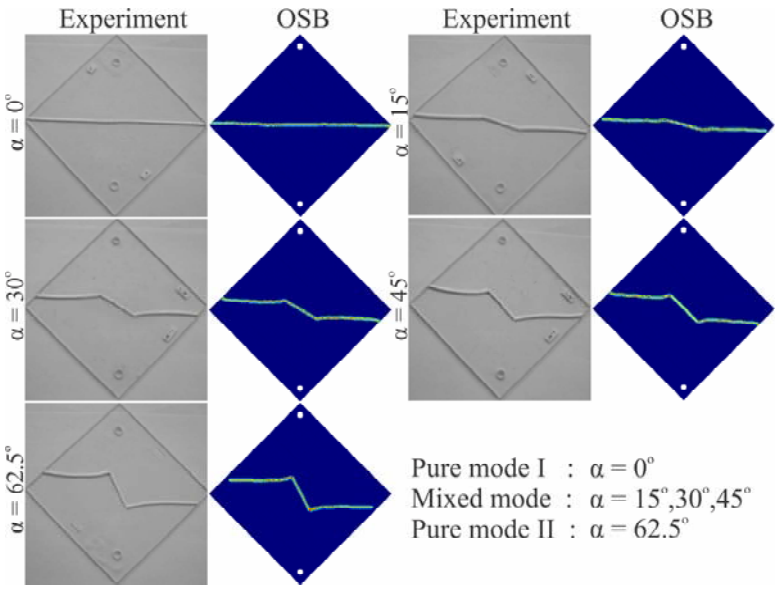

Figure 9) Comparison of the final crack path of the experiments and OSB results for DLSP specimens

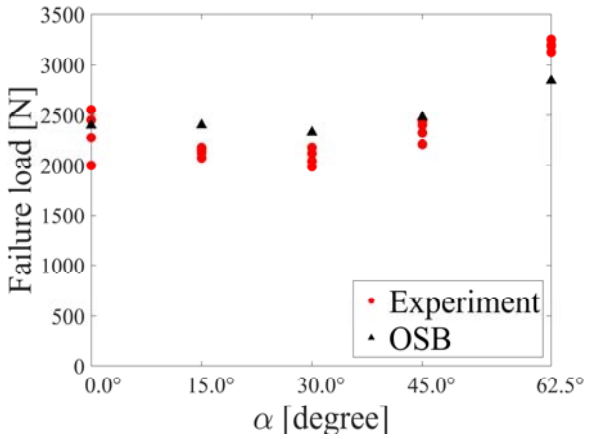

Figure 10) Comparison of the Failure load of the experiments and OSB results for DLSP specimens

3.3 Stop-hole combinations under uniaxial loading

In this section, different combinations of stop-holes are applied to a PMMA plate, with dimensions *L x W= 50mm x 50mm* and material properties given in Table 2, to strengthen the plate against crack propagation under tensile loading condition. A pre-existing crack with a length of *25 mm* is located at the left-middle part of all geometries (*Figure 11*). The geometries are then subjected to a velocity boundary condition with a crosshead velocity of *5 m/s*, representing a uniaxial loading at the top and bottom boundaries. All the analyses are performed for the differential time-step of $dt = 4.0x10^{-8}$ *s*, which is lower than the stable *dt* values proposed in Eq. (16). To obtain a fine PD model 500×500 material points are used in the discretization of the plate domain.

Firstly, the geometry with no hole (*Figure 11a)* is solved to have a reference case about crack dynamics in the body and to determine the time-steps for the start of crack propagation and complete rupture. As a result, the crack propagation starts approximately after 500^{th} time-step and eventually the complete rupture happens after nearly *1650* time-steps, which are considered as the reference of crack propagation interval for the following analyses.

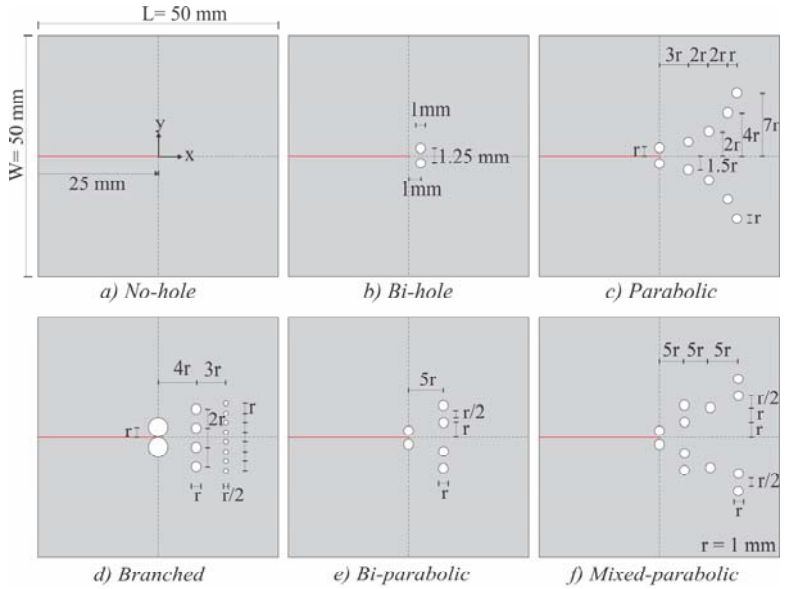

Figure 11) Geometric properties of stop-hole combinations under shear loading with r = 1 mm

Six different combinations of stop-holes, namely *No-hole, Bi-hole*, *Parabolic*, *Branched*, *Bi-parabolic* and *Mixed-parabolic* cases, are considered in the plate domain for toughness enhancement (*Figure 11*). A similar case to the *Bi-hole* combination was also solved by Vazic et al. [41], where the authors used two horizontal micro-cracks in order to investigate the influence of micro-cracks on main-crack dynamics. When the diameters of the applied holes are significantly small, holes and micro-cracks behave geometrically alike each other. However, if the diameters of the holes are large enough, the strain energy concentration is dispersed along the perimeter of the holes, which is in contrary to the case of micro-cracks, where the strain energy concentration occurs at the singular crack-tips. Therefore, stop-holes can cause a decrease in the average velocity of the main crack propagation as opposed to the particular case studied by Vazic et al. [41] where two parallel micro-cracks near the main crack tip accelerated the crack propagation.

The six different cases are compared with each other by means of crack growth rate for every *50* time-steps in *Figure 12*. It is clear from the graph that almost every combination of holes caused a delay in crack initiation time. The slopes of the lines in the graph imply the average velocity of crack propagation with the unit of mm/time-step. A relatively higher average propagation velocity is seen for some combinations of stop-holes at some portion of the graph. A higher crack propagation velocity indicates that the crack experiences a time-dependent acceleration between the adjacent time-steps due to the presence of the holes near the crack tip.

In fact, the presence of a hole in a body has two major effects on crack dynamics: (1) the accelerating effect, and (2) arresting effect. When a crack gets close enough to a hole, it tends to run to the hole with a continuously growing velocity until it joins the hole. This can be referred to as "accelerating effect". Once the crack joins a hole, it relaxes for a while by releasing its energy. This relaxation causes a decrease in the average propagation velocity of the crack, which can be referred to as "arresting effect". The accelerating and arresting effects of stop-holes can be seen between *400th* and *550th* time-steps for the *No-hole*, *Bi-hole* and *Parabolic* geometries in *Figure 12b*. The holes are located *1mm* ahead of the crack tip in *Bi-hole* geometry, thus the crack in this region accelerates towards the hole for the *1mm* distance. Hence, in this region the crack propagation velocity of *Bi-hole* geometry is higher than the one encountered in *No-hole* geometry. On the other hand, the first two holes are adjacent to the crack tip in *Parabolic* geometry and no distance is present for the crack to accelerate. Therefore, only the arresting effect of the holes exists in this region, causing a decrease in average velocity of the crack propagation.

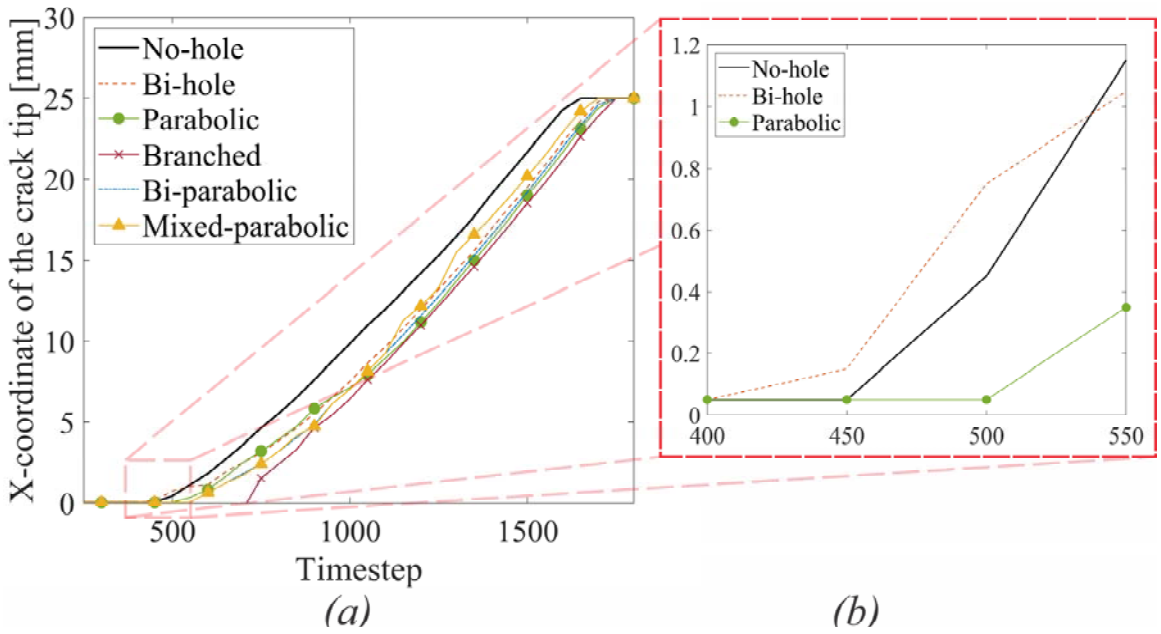

Figure 12) The graph of crack propagation vs time-step for No-hole, Bi-hole, Parabolic, Branched, Bi-parabolic and Mixed-parabolic stop-hole combinations

Figure 13 shows the evolution and the length of the cracks along with the branching effect at *800th*, *1200th* and *1600th* time-steps for the listed geometries. The geometries shown in *Figure 13* are zoomed into the failure zone, given that no failure has been detected in other regions of the plate. As shown in this figure, stop-holes can also affect the propagation angle of the cracks located in its neighborhood. This effect is extremely seen in the case of parabolic geometry, in which the crack has propagated towards the fourth hole with an angle of almost 90 degrees while the rest of the crack propagation is almost horizontal.

Furthermore, the Branched combination of stope-holes, so far, has proven to have the highest impact on material toughness (*Table 3*). Although the average propagation velocity between

800th and 1600th time-step of the Branched combination is the same with the one in No-hole combination, the branched combination has a higher effect on delaying the initiation time of crack propagation (almost 50%). This effect is the opposite in Bi-hole and relatively lower in Bi-parabolic and Mixed-parabolic combinations. In the Bi-hole geometry, despite its earlier initiation time, the average velocity of the crack propagation is much lower than the one in No-hole geometry, which causes a high toughening effect. On the other hand, Mixed-parabolic combination causes a relatively higher average propagation velocity between the previously mentioned time-steps. However, the total arresting effects in this geometry is higher than the total accelerating effects, which literally causes an increase in material toughness. Moreover, the parabolic combination causes a relatively higher delay in initiation time of the crack propagation and causes the lowest crack propagation velocity, leading to a second-high toughening effect. However, the precise implementation of this geometry can be challenging. On the other hand, the branched geometry is much easier to implement. In summary, it can be stated that the Branched geometry has the highest effect on material toughness and the lowest material cost with an average rate of reproducibility (*Table 4*).

Table 3) Summary of the crack dynamics of the geometries under tensile loading

	Crack propagation initiation time-step	X-coordinate of the crack tip at 800th time-step [mm]	X-coordinate of the crack tip at 1600th time-step [mm]	Average velocity between 800th and 1600th time-steps [mm/time-step]	Difference in average velocity with respect to No-hole	Delay in crack propagation initiation time with respect to No-hole	Difference in crack propagation length with respect to No-hole after 1600 time-steps
No-hole	480	5.55	24.25	0.0234	-	-	-
Mixed-parabolic	580	3.25	22.85	0.0245	4.81%	20.83%	-5.77%
Bi-hole	450	3.85	22.25	0.0230	-1.60%	-6.25%	-8.25%
Bi-parabolic	580	3.25	21.95	0.0234	0.00%	20.83%	-9.48%
Parabolic	540	3.95	21.65	0.0221	-5.35%	12.50%	-10.72%
Branched	720	2.45	21.15	0.0234	0.00%	50.00%	-12.78%

Table 4) Comparison of the geometries under tensile loading

	Reproducibility	Material Cost	Toughness Enhancement
No-hole	★★★★★	★★★★★	
Mixed-parabolic	★½	★½	★★
Bi-hole	★★★★	★★★★	★★½
Bi-parabolic	★★★½	★★★	★★★
Parabolic	★	★½	★★★½
Branched	★★½	★	★★★★★

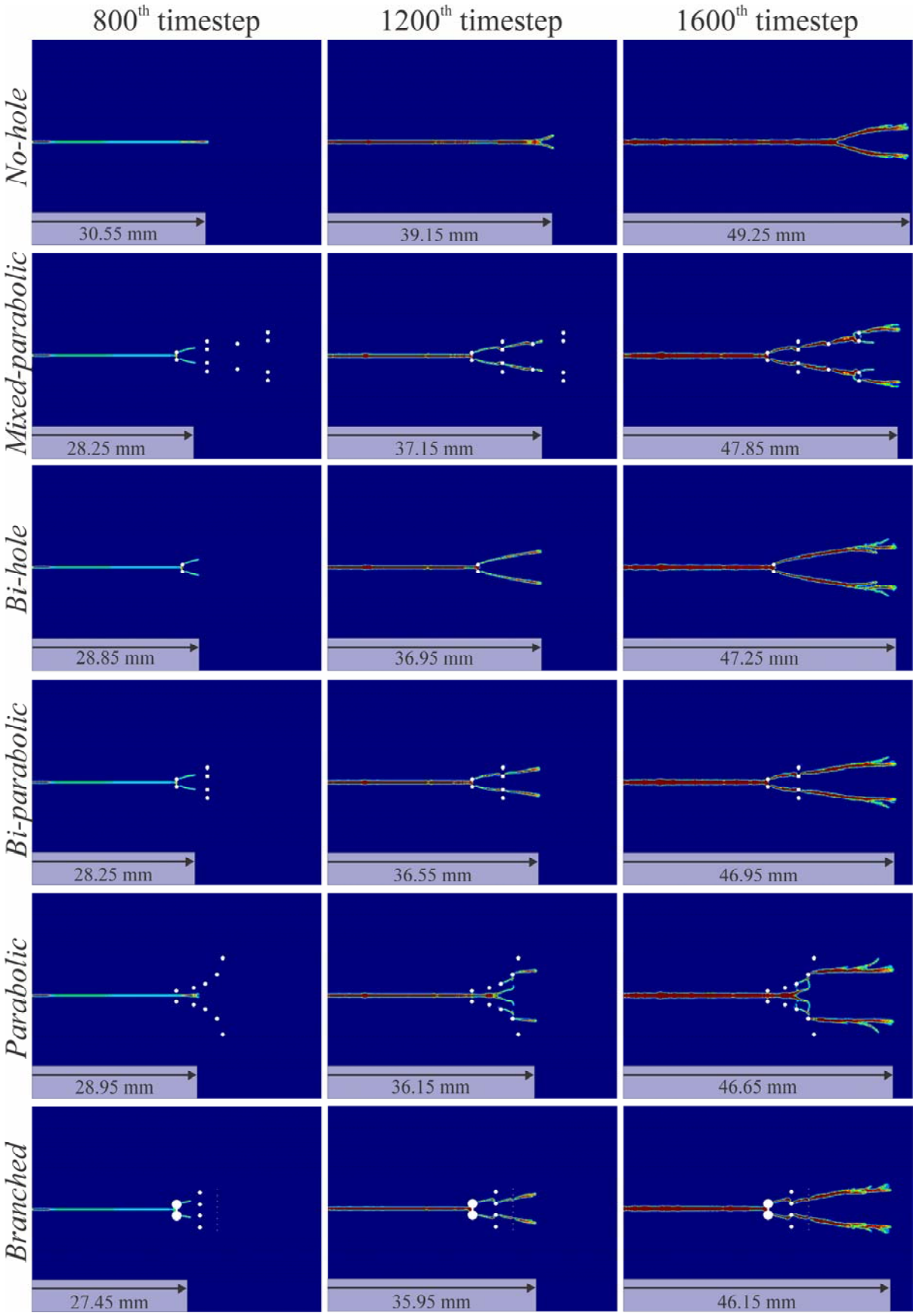

Figure 13) Crack length and branching effects of the geometries under tensile loading after 800th, 1200th and 1600th timesteps

3.4 Stop-hole combinations under shear loading

In this section, a plate of dimensions *50 mm x 50 mm* is analysed under velocity shear loading of *5 m/s* at the upper boundary, while the lower boundary is fixed. The material properties of the plate are same as the one used in the previous case. An initial crack with length of *L/4 (12.5 mm)* is located at the central left portion of the plate as shown in *Figure 14*. For all the analyses carried out in this section the time step size is taken as $dt=1.064x10^{-7}\ s$ which is the stable time step size calculated from Eq. (16). The breakage of the bonds is permitted under both tension and compression conditions with the equal magnitude of the critical stretch.

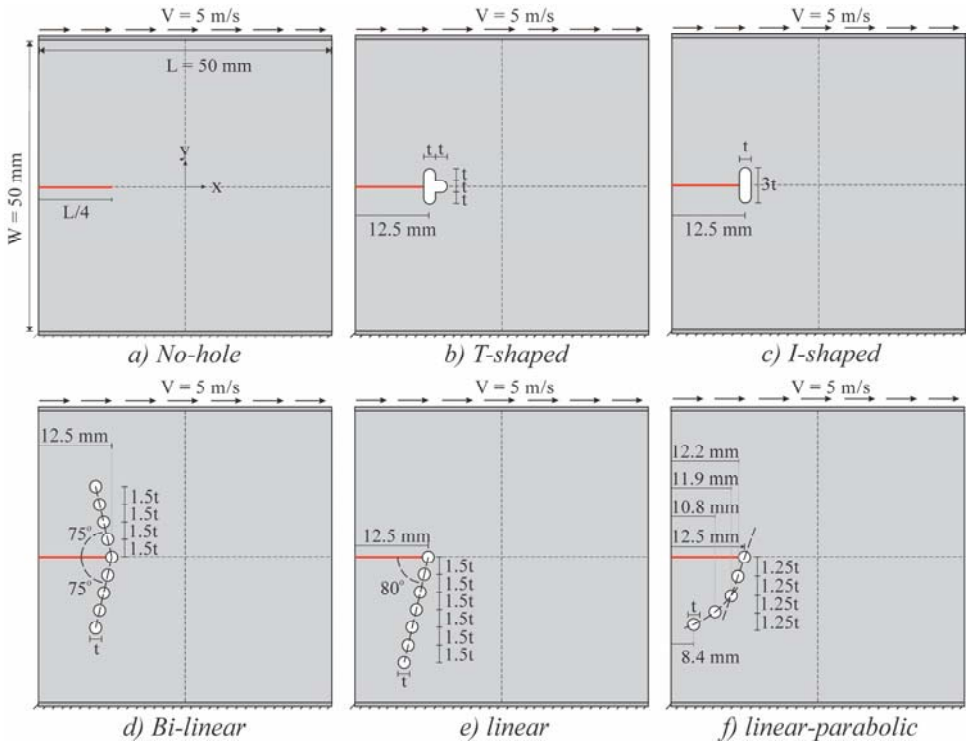

Figure 14) Geometric properties of the plates under shear boundary condition, with t=2 mm

To account for the total failure of the body, we consider the crack propagation lengths in both x- and y-directions. The contours of the displacements and failure are depicted in *Figure 15* for *No-hole* geometry after *1350* time-steps. Two new crack branches are formed in the body during the loading process, namely the lower and upper branches (*Figure 15*a). The lower crack branch is due to the internal tensile force caused by the boundary condition, whereas the upper crack branch is formed because of the compression effect of the loading on upper portion of the plate.

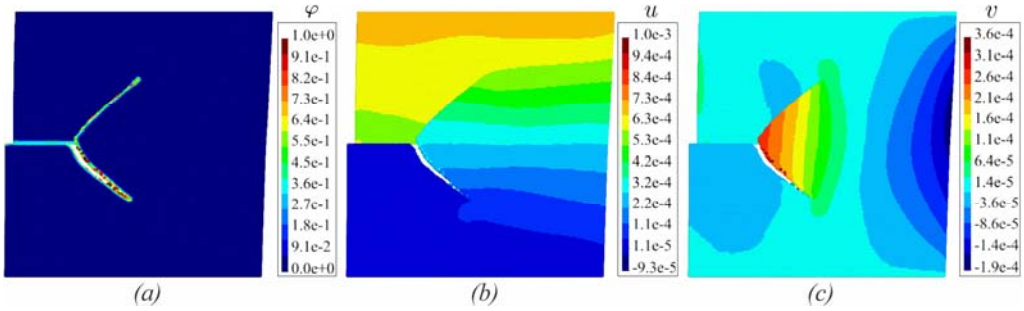

Figure 15) Counterplot of a) damage, b) displacement in x-direction [m] and c) displacement in y-direction [m] of No-hole geometry at 1350th time-step

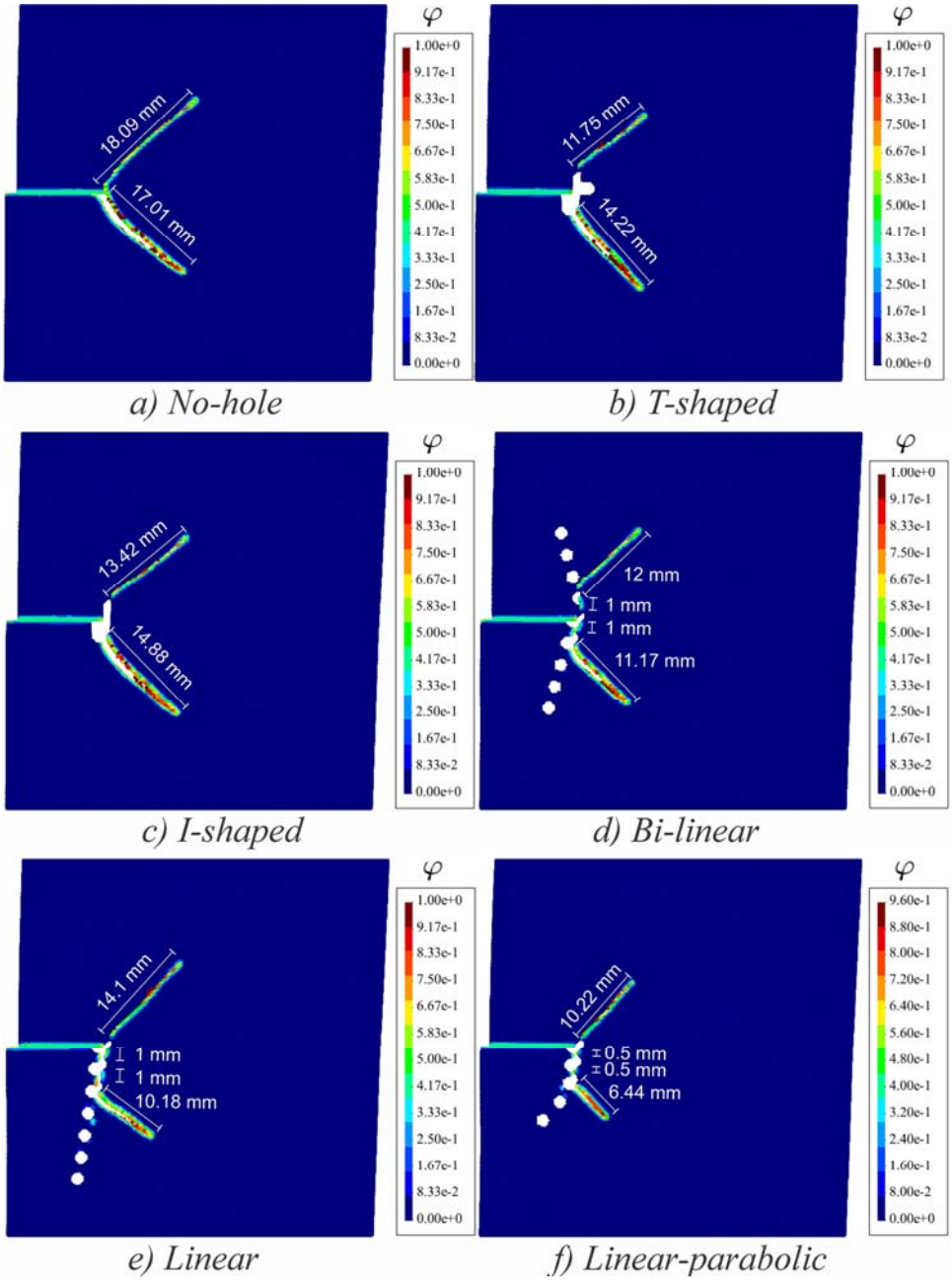

Figure 16) Crack surface and propagation length of the geometries under shear loading at 1350th time-step

In *Figure 16,* the crack propagations are shown for *No-hole, T-shaped, I-shaped, Bi-linear, Linear and Linear-parabolic* geometries. In order to define a reference failure state for toughness enhancement comparison, we define two different failure scale parameters: (1) total split length of material and (2) total failure length of material. To measure the total split length, the length of the split surface between different parts of plate is considered. Herein, this includes the length of the propagated crack as well as any other defect where the split surface passes through (e.g., the length of the first three upper holes in *Linear* and *Linear-parabolic* geometries). In other words, a total split length can be considered as a measure of the global failure of a material for which all defects existing in the body are taken into account. On the

other hand, a total failure length can be considered as the total length of the surface where the bonds between material points has failed due to exceeding the critical stretch (i.e. local failure). The variation of the above failure parameters against every incremental *50* time-steps are plotted in *Figure 17* for each geometry.

A summary of the crack dynamics in the above geometries is also given in *Table 5*, from which it can be seen that all the listed geometries have caused a significant amount of increase in the strength of the material. This toughening effect can be seen in the shape of a decrease in the average propagation velocity and/or a delay in the propagation initiation time. It is worthy to notice that almost every linear combinations of the circular stop-holes have a decreasing effect on the average velocity of the propagation, eventually causing a relatively higher toughness enhancement. However, the toughness enhancement in the T-shaped and I-shaped geometries are largely seen in the form of the delay in initiation time of the propagation. The toughening effect is the highest in Linear-parabolic combination due to the presence of both of the situations mentioned above. Furthermore, the Bi-linear combination of stop-holes causes the highest decrease in material cost, with a second-high toughening effect. In fact, the implementation of the Bi-linear combination of stop-holes is more economic and much easier than that of the Linear-parabolic combination (

Table 6).

Table 5) Summary of the crack dynamics of the geometries under shear loading

	Crack initiation time-step	Total split at initiation time-step [mm]	Total split at 1400th time-step [mm]	Average velocity of the propagation [mm/time-step]	Delay in crack propagation initiation time with respect to No-hole	Difference in average velocity with respect to No-hole	Difference in crack propagation length with respect to No-hole after 1400 time-steps
No-hole	950	2.19	40.05	0.0841			
T-shaped	1050	6.5	37.53	0.0887	10.53%	5.38%	-6.29%
I-shaped	1050	6.81	40.014	0.0949	10.53%	12.76%	-0.09%
Bi-linear	950	5.54	37.086	0.0701	0.00%	-16.68%	-7.40%
Linear	850	5.54	38.101	0.0592	-10.53%	-29.63%	-4.87%
Linear-parabolic	1100	8.27	30.428	0.0739	15.79%	-12.21%	-24.02%

Table 6) Comparison of the geometries under shear loading

	Reproducibility	Material Cost	Toughness Enhancement
No-hole	★★★★★	★★★★★	
I-shaped	★★★★	★★☆	★
Linear	★★★	★☆	★★
T-shaped	★★★☆	★★	★★☆
Bi-Linear	★★☆	★	★★★
Linear-parabolic	★	★★	★★★★★

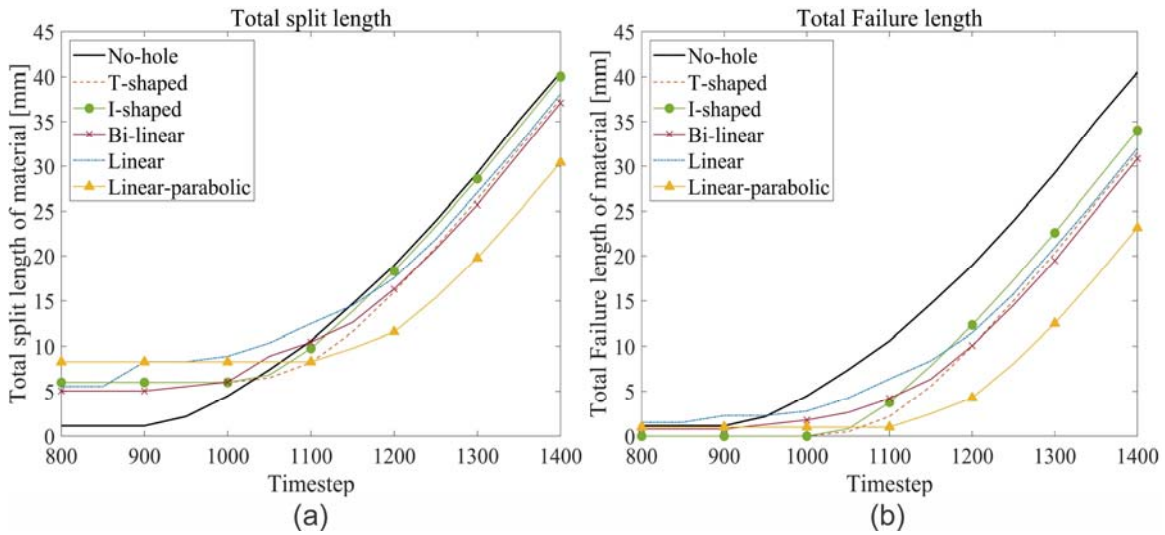

Figure 17) Graphs of a) total split length and b) total failure length of material vs time-step for the geometries under shear loading

3.5 Effects of the distance of stop-holes from the crack-tip on crack dynamics

In this section, the effect of the distance of stop-holes from the crack tip is investigated under the tensile loading. For this purpose, a plate with *L x W=50mm x 25mm* dimensions having a pre-existing crack with a length of *L/5 (10 mm)* located at its central left part is analysed. The material properties of the plate are given in *Table 7*. The distance between material points, *dx*, is taken as *0.25 mm*. The plate is subjected to a uniaxial velocity boundary condition of *+150 mm/s* and *-150 mm/s* at its upper and lower boundaries, respectively. As a first approach, a circular hole of diameter *D = 2 mm* is applied to the plate at a distance, *d*, from the crack tip (*Figure* 18*a*). Eq. (16) is used to ensure a time-step size not higher than the stable one.

Table 7) Material properties of the plate with dimensions of 50 mm x 25 mm

E	ν	P	G_c
3.24 GPa	0.35	1190 Kg/m^3	200 J/m^2

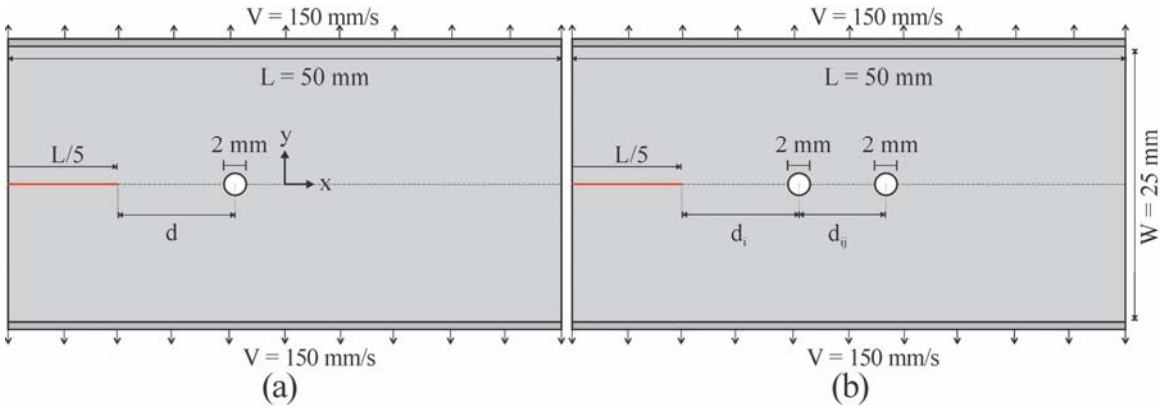

Figure 18) Geometric properties of the plate with a) one and b) two holes under uniaxial tension

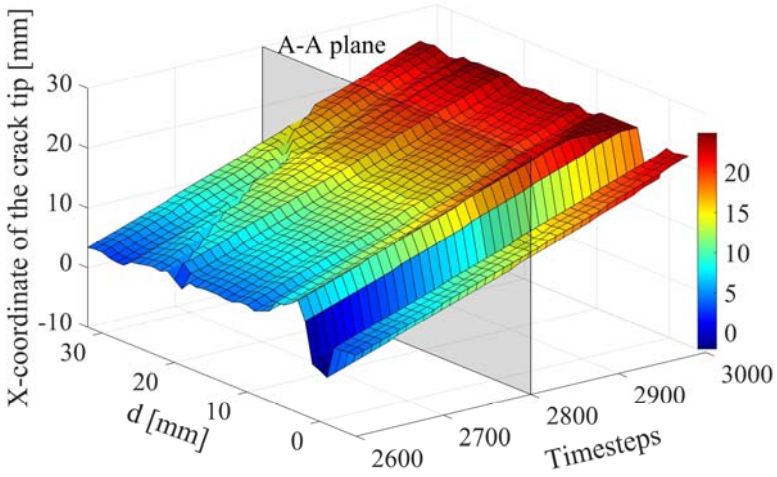

Figure 19) Graph of the change in position of the crack tip vs time-step for various values of d for the plate with one hole

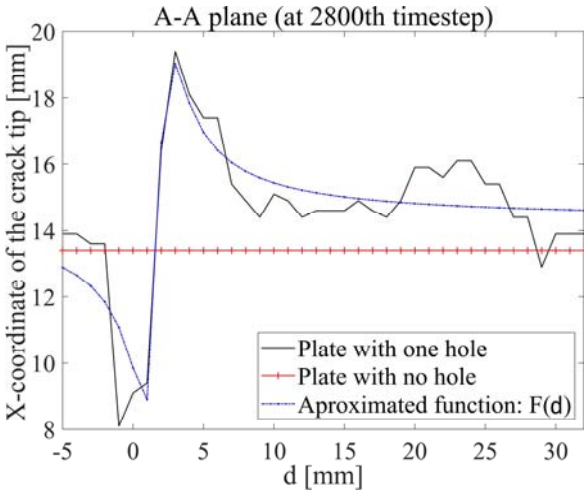

Figure 20) The graph of the change in position of the crack tip at 2800th time-step vs d for the plate with one hole

The presence of the hole causes the crack to have a position dependent velocity once the crack-tip gets close enough to the hole. Depending on initial relative position of the crack-tip from the hole, the average propagation velocity of the crack can be increasing, decreasing or constant. *Figure 19* shows the position of the crack-tip plotted versus every 10 time-steps for various values of d. A singular stop-hole causes a decrease in average propagation velocity of the crack if it is implemented to the material in such a way that the relative position of the crack tip falls inside the perimeter of the hole (i.e., $|d| \leq \frac{D}{2}$). This effect is the highest when the hole is located ahead of the crack at the exact tangency of the crack tip (i.e., $d = -\frac{D}{2}$). However, when the distance between the hole and the initial crack tip is higher (i.e., $d > \frac{D}{2}$), the hole will affect the material toughness in a negative manner by increasing the average crack propagation velocity. Interestingly, this effect is recorded as a decreasing function of d after a certain distance (e.g. d ≈ 2D for the present case). Thus, it can be concluded that a certain constant influence range of μ exists for a hole such that; whenever a crack enters the μ-range of the hole it starts to accelerate whereas for any distance beyond this μ-range, the effect of the hole on crack dynamics is zero.

The position of the crack-tip with respect to the distance, *d*, plotted in *Figure 20* can be approximated through the curve fitting with a function of:

$$F(d) = \frac{14.3d^2 - 39.730d + 37.68}{d^2 - 3.448d + 3.823} \tag{17}$$

where *F(d)* denotes the position of the crack tip at an instant of time (2800th time-step in the present case). If the distance, *d*, is significantly large, i.e., $d \to \infty$, the function approaches to the constant value of $F(d) = 14.3$ [mm]. This reveals the fact that if the hole is located far enough from the crack tip, the hole, independent from its position, will accelerate the crack for

a constant distance if and only if the crack enters the μ-range. This distance can be related with the μ-acceleration as follows:

$$14.3 - X_c = \frac{1}{2} a_\mu t_\mu^2 \tag{18}$$

where X_c is the position of crack tip at the same instant of time for the situation in which no stop-hole exists in the body (13.44 mm for the present case). The parameters, a_μ and t_μ, are named as the μ-acceleration (the acceleration caused by the hole) and μ-time (the amount of time of μ-acceleration), respectively. Consequently, the *F(d)* function can be used to measure the amount of the accelerating effect of the stop-holes on crack propagation.

However, the crack dynamics can also be altered by number of holes in the body. To investigate this effect, a second stop-hole is placed at a distance of d_{ij} from the first hole (*Figure 18b*). For this purpose, a rupture corresponding to *80%* of the plate (equivalently, the crack tip reaches the coordinate of $x = 15\ mm$) is taken as the basis of comparison. *Figure 21* clearly indicates that the toughening effect is the highest for the values of d_i and $d_{ij} \in [0 - 1]$. Furthermore, for the higher values of d_i and d_{ij}, a decrease in the strength of the material is observed. This weakening effect, however, approaches a constant value when d_i and d_{ij} get larger. Additionally, as can be seen from *Figure 22*, a strengthening effect at the small values of d_i and an abating weakening effect at the high values of $d_{ij} \in [4mm - 10\ mm]$ is clearly noticeable, hence leading to a higher toughness. This also indicates that the toughening effect of a hole placed near the crack tip is much higher than the weakening effect of a hole located in far-hand regions. On the other hand, for larger values of d_i, the variation of d_{ij} has a very low impact on the strength of the material. This well agrees with our previous findings on the μ-*ranges* of stop-holes where it was stated that for any large value of d, any stop-hole regardless of the distance d will accelerate the crack propagation for a constant distance.

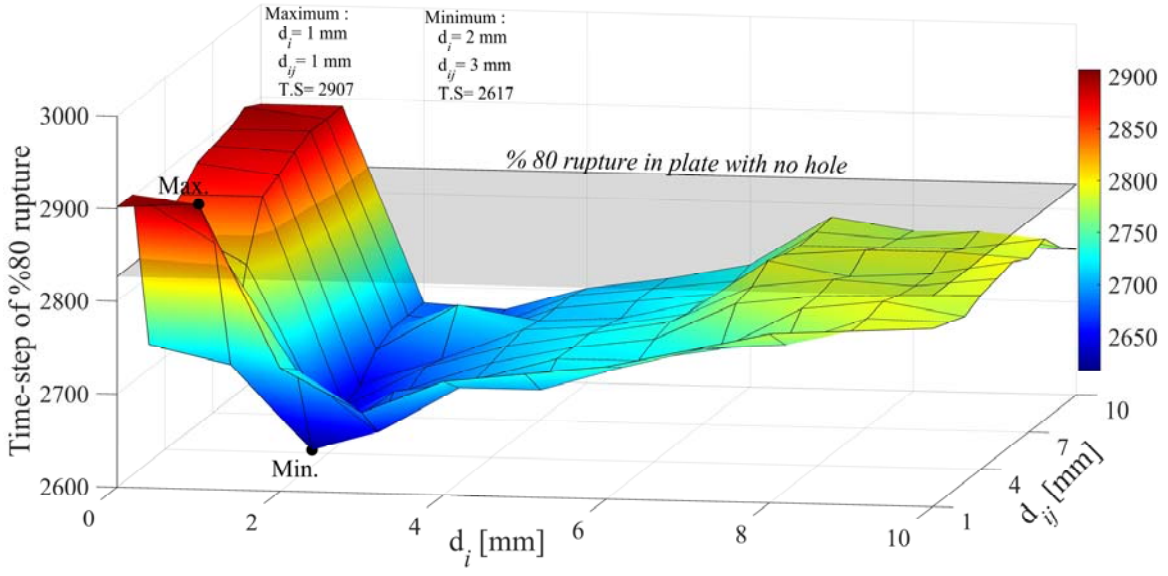

Figure 21) Graph of the change in time-steps of the %80 rapture of the plate with two holes vs d_i and d_{ij}

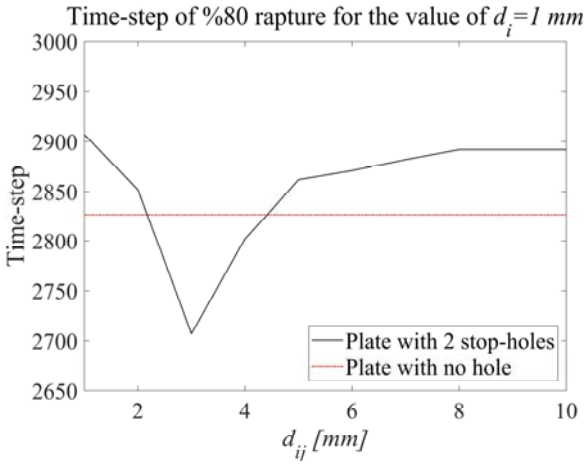

Figure 22) The variation of the time-step of the %80 rupture vs d_{ij} of the plate with two stop-holes

It should be noted that the above conclusions were made only by taking into account the horizontal relative positions of the initial crack-tip and holes. A more detailed study can be carried out, as the crack dynamics is affected not only by the horizontal distance of the holes but also the vertical distance and diameter, *D*, of the holes as well as the initial pre-existing crack length, which are beyond the extent of this paper.

4. Conclusions

In the scope of this study, the effects of various linear/non-linear combinations of stop-holes on toughness enhancement in brittle materials are investigated under tensile and shear loadings by performing ordinary state-based peridynamic (OSB-PD) analysis. The numerical algorithm is assessed by solving benchmark cases with various facture modes and the results are

compared with the experimental-numerical finding of literature [9,49]. It is demonstrated the OSB-PD can predict very similar final fracture patterns observed in the experiments for mode-I, mode-II, and mixed mode I-II loading conditions [49]. Additionally, the accuracy of presented approach is further validated with respect to experiments and dynamic phase-field method for crack propagation in porous media. The OSB-PD is shown to produce superior final fracture pattern than that of phase-field method. Furthermore, Broek [5] and Miyagawa et al. [6] reported in their experimental studies that a crack is attracted towards any nearby hole in a porous media. This important physical phenomenon is accurately captured by our numerical results.

Having validated the proposed algorithm and its numerical implementation on various challenging problems, we have studied further complex problems that involves various stop-holes combinations for toughness enhancement under tensile and shear loadings. The toughening effects of the proposed stop-hole configurations are evaluated referring to the total split and failure lengths. These stop-holes combinations are shown to be very effective for decreasing the total split length, the total failure length and the average propagation velocity of the cracks, hence increasing the material toughness. The effect of the distance of multiple stop-holes from the crack tip is also investigated. It is observed that every stop-hole has an influence domain (i.e., the μ-range) beyond which the crack dynamics is not significantly affected. It is noted that when the stop-hole intercepts the crack-tip, the material toughening is maximized. On the other hand, if the stop-hole is located in the far field of the crack tip, the material toughness decreases. Additionally, it is concluded from the analysis with two stop-holes that the toughening effect is maximized when both stop-holes are placed near crack tip. Depending on the distance between two holes, material toughness can be tailored. Finally, the influence of drilling stop-holes on labour and material cost is also compared for different stop-hole configurations. Hence, this comparison can provide valuable information for addressing time-cost-trade off problems

Acknowledgement

The financial support provided by the Scientific and Technological Research Council of Turkey (TUBITAK) under the grant No: 217M207 is greatly acknowledged.

References

[1] L. Ceriolo, A. Di Tommaso, Fracture mechanics of brittle materials : An historical point of view, 2nd Int. PhD Symp. Civ. Eng. (1998) 207–214.

[2] H. Cui, W. Wang, A. Li, M. Li, S. Xu, H. Liu, Failure analysis of the brittle fracture of a thick-walled 20 steel pipe in an ammonia synthesis unit, Eng. Fail. Anal. 17 (2010) 1359–1376. https://doi.org/10.1016/j.engfailanal.2010.04.002.

[3] T. Moan, J. Amdahl, Catastrophic failure modes of marine structures, in: Struct. Fail., 1989: pp. 463–510.

[4] V. Infante, J.M. Silva, M.A.R. Silvestre, R. Baptista, Failure of a crankshaft of an aeroengine: A contribution for an accident investigation, Eng. Fail. Anal. 35 (2013) 286–293. https://doi.org/10.1016/j.engfailanal.2013.02.002.

[5] D. Broek, Practical Problems, in: Elem. Eng. Fract. Mech., Marinus Nijhoff, 1982: pp. 347–376.

[6] H. Miyagawa, H. Nisitani, Retardation of Fatigue Crack Propagation Due to Additional Holes or Indentations in Plate Specimens, Bull. JSME. 28 (1985) 84–0318. https://doi.org/10.1299/jsme1958.28.2219.

[7] M. Isida, On the determination of stress intensity factors for some common structural problems, Eng. Fract. Mech. 2 (1970) 61–79. https://doi.org/10.1016/0013-7944(70)90030-5.

[8] R.S. Yang, C.X. Ding, L.Y. Yang, P. Xu, C. Chen, Hole Defects Affect the Dynamic Fracture Behavior of Nearby Running Cracks, Shock Vib. 2018 (2018). https://doi.org/10.1155/2018/5894356.

[9] J. Carlsson, P. Isaksson, Crack dynamics and crack tip shielding in a material containing pores analysed by a phase field method, Eng. Fract. Mech. 206 (2019) 526–540. https://doi.org/10.1016/j.engfracmech.2018.11.013.

[10] G.A. Francfort, J.J. Marigo, Revisiting Brittle Fracture as an Energy Minimization Problem, J. Mech. Phys. Solids. 46 (1998) 1319–1342. https://doi.org/10.1016/S0022-5096(98)00034-9.

[11] R.S. Qin, H.K. Bhadeshia, Phase field method, Mater. Sci. Technol. 26 (2010) 803–811. https://doi.org/10.1179/174328409X453190.

[12] S.A. Silling, Reformulation of elasticity theory for discontinuities and long-range forces, J. Mech. Phys. Solids. 48 (2000) 175–209. https://doi.org/10.1016/S0022-5096(99)00029-0.

[13] E. Oterkus, E. Madenci, Peridynamic analysis of fiber-reinforce materials, Mech. Mater. Struct. 7 (2012).

[14] S. Oterkus, E. Madenci, A. Agwai, Fully coupled peridynamic thermomechanics, J. Mech. Phys. Solids. 64 (2014) 1–23. https://doi.org/10.1016/j.jmps.2013.10.011.

[15] S. Oterkus, E. Madenci, A. Agwai, Peridynamic thermal diffusion, J. Comput. Phys. 265 (2014) 71–96. https://doi.org/10.1016/j.jcp.2014.01.027.

[16] D. De Meo, C. Diyaroglu, N. Zhu, E. Oterkus, M.A. Siddiq, Modelling of stress-corrosion cracking by using peridynamics, Int. J. Hydrogen Energy. 41 (2016) 6593–6609. https://doi.org/10.1016/j.ijhydene.2016.02.154.

[17] A. Kefal, A. Sohouli, E. Oterkus, Topology optimization of cracked structures using peridynamics, Contin. Mech. Thermodyn. (2019). https://doi.org/10.1007/s00161-019-00830-x.

[18] A. Sohouli, A. Kefal, A. Abdelhamid, M. Yildiz, A. Suleman, Continuous Density-Based Topology Optimization of Cracked Structures Using Peridynamics, Struct. Multidiscip. Optim. (n.d.). http://dx.doi.org/10.1007/s00158-020-02608-1.

[19] M. Ghajari, L. Iannucci, P. Curtis, A peridynamic material model for the analysis of dynamic crack propagation in orthotropic media, Comput. Methods Appl. Mech. Eng. 276 (2014) 431–452. https://doi.org/10.1016/j.cma.2014.04.002.

[20] H. Wang, Y. Xu, D. Huang, A non-ordinary state-based peridynamic formulation for thermo-visco-plastic deformation and impact fracture, Int. J. Mech. Sci. 159 (2019) 336–344. https://doi.org/10.1016/j.ijmecsci.2019.06.008.

[21] V. Diana, S. Casolo, A full orthotropic micropolar peridynamic formulation for linearly elastic solids, Int. J. Mech. Sci. 160 (2019) 140–155. https://doi.org/10.1016/j.ijmecsci.2019.06.036.

[22] S.A. Silling, E. Askari, A meshfree method based on the peridynamic model of solid mechanics, Comput. Struct. 83 (2005) 1526–1535. https://doi.org/10.1016/j.compstruc.2004.11.026.

[23] E. Madenci, A. Kefal, M. Dorduncu, A. Barut, M. Yildiz, Isogeometric analysis using peridynamics and XFEM, in: AIAA/ASCE/AHS/ASC Struct. Struct. Dyn. Mater. Conf. 2018, American Institute of Aeronautics and Astronautics, 2018: pp. 1–21. https://doi.org/10.2514/6.2018-1464.

[24] S.A. Silling, Linearized theory of peridynamic states, J. Elast. 99 (2010) 85–111. https://doi.org/10.1007/s10659-009-9234-0.

[25] E. Madenci, S. Oterkus, Ordinary state-based peridynamics for plastic deformation according to von Mises yield criteria with isotropic hardening, J. Mech. Phys. Solids. 86 (2015) 192–219. https://doi.org/10.1016/j.jmps.2015.09.016.

[26] S.A. Silling, M. Epton, O. Weckner, J. Xu, E. Askari, Peridynamic states and constitutive modeling, J. Elast. 88 (2007) 151–184. https://doi.org/10.1007/s10659-007-9125-1.

[27] E. Madenci, E. Oterkus, Peridynamic theory and its applications, Springer, 2014. https://doi.org/978-1-4614-8465-3.

[28] B. Kilic, Peridynamic Theory for Progressive Failure Prediction in Homogeneous and Heterogeneous Materials, The University of Arizona, 2008.

[29] E. Askari, F. Bobaru, R.B. Lehoucq, M.L. Parks, S.A. Silling, O. Weckner, Peridynamics for multiscale materials modeling, J. Phys. Conf. Ser. 125 (2008). https://doi.org/10.1088/1742-6596/125/1/012078.

[30] Y.D. Ha, F. Bobaru, Studies of dynamic crack propagation and crack branching with peridynamics, Int. J. Fract. 162 (2010) 229–244. https://doi.org/10.1007/s10704-010-9442-4.

[31] F. Bobaru, G. Zhang, Why do cracks branch? A peridynamic investigation of dynamic brittle fracture, Int. J. Fract. 196 (2015) 59–98. https://doi.org/10.1007/s10704-015-0056-8.

[32] H. Pashazad, M. Kharazi, A peridynamic plastic model based on von Mises criteria with isotropic, kinematic and mixed hardenings under cyclic loading, Int. J. Mech. Sci. 156 (2019) 182–204. https://doi.org/10.1016/j.ijmecsci.2019.03.033.

[33] B. Kilic, E. Madenci, An adaptive dynamic relaxation method for quasi-static simulations using the peridynamic theory, Theor. Appl. Fract. Mech. 53 (2010) 194–204. https://doi.org/10.1016/j.tafmec.2010.08.001.

[34] D. Yang, X. He, S. Yi, X. Liu, An improved ordinary state-based peridynamic model for cohesive crack growth in quasi-brittle materials, Int. J. Mech. Sci. 153–154 (2019) 402–415. https://doi.org/10.1016/j.ijmecsci.2019.02.019.

[35] E. Oterkus, E. Madenci, O. Weckner, S. Silling, P. Bogert, A. Tessler, Combined finite element and peridynamic analyses for predicting failure in a stiffened composite curved panel with a central slot, Compos. Struct. 94 (2012) 839–850. https://doi.org/10.1016/j.compstruct.2011.07.019.

[36] S.A. Silling, R.B. Lehoucq, Convergence of Peridynamics to Classical Elasticity Theory, J. Elast. 93 (2008) 13–37. https://doi.org/10.1007/s10659-008-9163-3.

[37] B. Kilic, E. Madenci, Coupling of Peridynamic Theory and The Finite Element Method, J. Mech. Mater. Struct. 5 (2010). https://msp.org/jomms/2010/5-5/jomms-v5-n5-p02-s.pdf.

[38] M. Imachi, S. Tanaka, M. Ozdemir, T.Q. Bui, S. Oterkus, E. Oterkus, Dynamic crack arrest analysis by ordinary state-based peridynamics, Int. J. Fract. (2020). https://doi.org/10.1007/s10704-019-00416-3.

[39] B. Florin, J.T. Foster, P.H. Geubelle, S.A. Silling, Handbook of Peridynamic Modeling, CRC press, 2016. https://doi.org/10.1002/zamm.201709792.

[40] A. Javili, R. Morasata, E. Oterkus, S. Oterkus, Peridynamics review, Math. Mech. Solids. 24 (2019) 3714–3739. https://doi.org/10.1177/1081286518803411.

[41] B. Vazic, H. Wang, C. Diyaroglu, S. Oterkus, E. Oterkus, Dynamic propagation of a macrocrack interacting with parallel small cracks, AIMS Mater. Sci. 4 (2017) 118–136. https://doi.org/10.3934/matersci.2017.1.118.

[42] M.F. Basoglu, Z. Zerin, A. Kefal, E. Oterkus, A computational model of peridynamic theory for deflecting behavior of crack propagation with micro-cracks, Comput. Mater. Sci. 162 (2019) 33–46. https://doi.org/10.1016/j.commatsci.2019.02.032.

[43] Z. qiu Fu, B. hai Ji, S. hui Xie, T. jia Liu, Crack stop holes in steel bridge decks: Drilling method and effects, J. Cent. South Univ. 24 (2017) 2372–2381. https://doi.org/10.1007/s11771-017-3649-8.

[44] R. Ghfiri, H.J. Shi, R. Guo, G. Mesmacque, Effects of expanded and non-expanded hole on the delay of arresting crack propagation for aluminum alloys, Mater. Sci. Eng. A. 286 (2000) 244–249. https://doi.org/10.1016/S0921-5093(00)00805-4.

[45] P.S. Song, Y.L. Shieh, Stop drilling procedure for fatigue life improvement, Int. J. Fatigue. 26 (2004) 1333–1339. https://doi.org/10.1016/j.ijfatigue.2004.04.009.

[46] M.S. Ferdous, K. Naka, C. Makabe, T. Miyazaki, A Review of Simple Methods for Arresting Crack Growth, Adv. Mater. Res. 1110 (2015) 185–190. https://doi.org/10.4028/www.scientific.net/amr.1110.185.

[47] M.R. Ayatollahi, S.M.J. Razavi, H.R. Chamani, Fatigue life extension by crack repair using stop-hole technique under pure mode-i and pure mode-ii loading conditions, Procedia Eng. 74 (2014) 18–21. https://doi.org/10.1016/j.proeng.2014.06.216.

[48] M. Fanni, N. Fouda, M.A.N. Shabara, M. Awad, New crack stop hole shape using structural optimizing technique, Ain Shams Eng. J. 6 (2015) 987–999. https://doi.org/10.1016/j.asej.2015.02.010.

[49] M.R. Ayatollahi, M.R.M. Aliha, Analysis of a new specimen for mixed mode fracture tests on brittle materials, Eng. Fract. Mech. 76 (2009) 1563–1573. https://doi.org/10.1016/j.engfracmech.2009.02.016.

[50] N. Kovvali, Theory and Applications of Gaussian Quadrature Methods, Synth. Lect. Algorithms Softw. Eng. 3 (2011) 1–65. https://doi.org/10.2200/S00366ED1V01Y201105ASE008.

[51] J.L. Lagrange, A. Boissonnade, V.N. Vagliente, Analytical Mechanics : Translated from the Mécanique analytique, novelle édition of 1811, Springer Netherlands, 1997.

[52] G. Qian, W.S. Lei, M. Niffenegger, V.F. González-Albuixech, On the temperature independence of statistical model parameters for cleavage fracture in ferritic steels, Philos. Mag. 98 (2018) 959–1004. https://doi.org/10.1080/14786435.2018.1425011.

[53] G. Qian, Y. Cao, M. Niffenegger, Y.J. Chao, W. Wu, Comparison of constraint analyses with global and local approaches under uniaxial and biaxial loadings, Eur. J. Mech. A/Solids. 69 (2018) 135–146. https://doi.org/10.1016/j.euromechsol.2017.12.006.

[54] G. Qian, W.S. Lei, L. Peng, Z. Yu, M. Niffenegger, Statistical assessment of notch toughness against cleavage fracture of ferritic steels, Fatigue Fract. Eng. Mater. Struct. 41 (2018) 1120–1131. https://doi.org/10.1111/ffe.12756.

[55] L. Lapidus, G.F. Pinder, Numerical Solution of PDEs in Science and Engineering, A Wiley-interscience Publication, 1999.

[56] H. Wang, X. Zhang, Y. Duan, Effects of drilling area temperature on drilling of carbon fiber reinforced polymer composites due to temperature-dependent properties, Int. J. Adv. Manuf. Technol. 96 (2018) 2943–2951. https://doi.org/10.1007/s00170-018-1810-7.